ADVANCED PHOTONICS RESEARCH
Open Access
www.adpr-journal.com

$CsSnBr_3$ and $Cs_3Bi_2Br_9$: Structural, Optical Characteristics, and Application in a Schottky Barrier Diode

Olusola Akinbami, Thelma Majola, Grace Nomthandazo Ngubeni, Kalenga Pierre Mubiayi, and Nosipho Moloto**

The search for alternatives to Pb-based perovskites, due to concerns about stability and toxicity, has led to the exploration of Pb-free options. Tin (Sn) and bismuth (Bi) are promising candidates, given their similar ionic radii to Pb and the isoelectronic nature of Pb^{2+} and Bi^{3+}, which suggest comparable chemical properties. Among these, $CsSnBr_3$ and $Cs_3Bi_2Br_9$ are relatively underexplored but offer lower toxicity and enhanced stability while demonstrating optoelectronic properties suitable for various applications. In this study, $CsSnBr_3$ and $Cs_3Bi_2Br_9$ nanocrystals are synthesized using a colloidal method and integrated into Schottky diodes. X-ray photoelectron spectroscopy analysis of the surface chemistry confirms improved thermal and phase stability compared to Pb-based perovskites. Schottky diode parameters, including ideality factor, barrier height, and series resistance are assessed using conventional thermionic emission, modified Cheung's, and Norde's models. The $Cs_3Bi_2Br_9$-based Schottky diode exhibits superior electrical performance with the lowest series resistance and optimal barrier height. Electrical impedance spectroscopy results indicated that $CsSnBr_3$ has higher resistances and lower capacitances than $Cs_3Bi_2Br_9$, reflecting lower charge carrier mobility and more defects, although the R_1C_1 regions in both materials demonstrated faster charge dynamics, making them ideal for high-speed applications.

1. Introduction

The quest for renewable energy sources has been a focal point of scientific research in recent years. Among the various renewable energy options, solar energy stands out due to its abundance and environmentally friendly nature.[1] Different solar cell technologies exist, but perovskite solar cells (PSCs) have emerged as particularly disruptive due to their rapid advancements in efficiency over a short period.[2] Despite their impressive performance, PSCs face significant stability challenges under ambient conditions and present environmental concerns, when lead (Pb) is used.[3] Consequently, research has increasingly focused on developing lead-free perovskites to address these issues.[4] Perovskites are generally represented by the formula ABX_3, where "A" is typically a large cation, "B" is a smaller cation, and "X" is either oxygen or a halide. Examples of such perovskites include $CaTiO_3$, $CH_3NH_3PbI_3$, and $CsPbBr_3$.[5,6] The crystal structure of perovskites is characterized by the "A" cation coordinating with 12 anions to form a cuboctahedral structure, while the "B" cation coordinates with 6 anions to form an octahedral structure.[7,8] Ideally, perovskites have a cubic structure, but deviations from this ideal can occur due to variations in the ionic radii of their constituent elements.[9,10]

The perovskite structure's versatility allows for the incorporation of numerous divalent cations from the periodic table, with tin (Sn) and bismuth (Bi) being among the most promising substitutes for lead.[11] Tin, with an atomic number of 50, shares similar chemical properties with lead due to their group association and nearly identical ionic radii (Sn: 0.115 nm, Pb: 0.117 nm).[11] This similarity enables tin to fit well into the "B" site of the perovskite crystal structure. Moreover, tin is considered less toxic than lead, as it is poorly absorbed by organisms, except in the case of certain toxic organotin compounds.[12] Bismuth, another potential lead substitute, has an atomic number of 83 and is in the same period as lead. The Bi^{3+} ion is isoelectronic with the Pb^{2+} ion, sharing similar electronic configurations.[13] However, bismuth is generally less toxic than lead, with bismuth compounds such as bismuth vanadate being used in cosmetics and pharmaceuticals for decades.[14] Bismuth-based perovskites often adopt the $A_3B_2X_9$ formula, forming stable, less-toxic materials ideal for replacing lead in various applications.

The application of perovskites in devices such as solar cells or sensors requires the integration of the perovskite semiconductor with other materials. The interfaces formed between these materials are critical, as they influence the electrical and transport properties of the devices. Schottky diodes, which are metal–semiconductor junction devices, demonstrate rectifying

O. Akinbami, T. Majola, G. N. Ngubeni, K. P. Mubiayi, N. Moloto
Molecular Sciences Institute, School of Chemistry
University of the Witwatersrand
Private Bag 3, Wits 2050, Johannesburg 2000, South Africa
E-mail: Kalenga.Mubiayi@wits.ac.za; Nosipho.Moloto@wits.ac.za

The ORCID identification number(s) for the author(s) of this article can be found under https://doi.org/10.1002/adpr.202300337.

DOI: 10.1002/adpr.202300337

behaviour similar to p–n junctions in traditional solar cells.[15] Understanding Schottky junctions provides insights into photovoltaic mechanisms, including charge separation and transport.[15] Schottky diodes have a built-in potential barrier at the metal–semiconductor interface that influences carrier dynamics, optimizing photogenerated carrier separation in solar cells.[16] Studying Schottky devices can reveal charge transport mechanisms like thermionic emission and tunneling, which are crucial for advanced solar cell designs. These devices also help in understanding and mitigating recombination losses in solar cells, enhancing their efficiency.[17] Their straightforward fabrication and characterization methods facilitate diagnostics and performance optimization in solar cells. Additionally, Schottky devices serve as models for metal–semiconductor interactions, aiding in the development of hybrid and advanced solar cell architectures.[18]

In sensor applications, Schottky diodes are valued for their high sensitivity and fast response times, making them ideal for detecting small signals and providing real-time data.[19] Their low forward voltage drop enhances energy efficiency, particularly in portable and battery-powered devices.[20] They perform effectively across a wide range of frequencies, which is beneficial for high-speed applications like RF and microwave detection.[21] Their good temperature stability ensures reliable performance under varying conditions, and their compact size allows for integration into miniaturized sensor designs, simplifying sensor circuit design and reducing complexity and cost.[22]

In this study, $CsSnBr_3$ and $Cs_3Bi_2Br_9$ perovskite nanocrystals (NCs) were investigated as semiconductors in the fabrication of Schottky diodes. Key diode parameters were analyzed using three models: the classical thermionic emission model, Cheung's method, and Norde's method.

2. Experimental Section

2.1. Chemicals

Bismuth bromide ($BiBr_3$, 98%), tin (II) bromide ($SnBr_2$ 99%), cesium carbonate (Cs_2CO_3 99%), oleylamine (OLA 70%), oleic acid (OA, 90%), toluene (95%), hexane (95%), acetone, ethanol, indium-doped tin oxide (ITO) coated glass slide (surface resistivity $\approx$8–12 $\Omega\,sq^{-1}$) were purchased from Sigma-Aldrich. Gold target (Au, 99.95%, 6.35 mm) was purchased from Alfa Aesar.

2.2. Synthesis of $CsSnBr_3$ and $Cs_3Bi_2Br_9$ Perovskite Nanocrystals

In a three-necked round bottom flask, 0.1 g cesium carbonate (Cs_2CO_3) was placed in 10 mL of oleic acid (OA) and heated to 150 °C for an hour under continuous stirring to thoroughly dissolve the Cs_2CO_3 and generate cesium oleate (CsOA) under the nitrogen flow. In another 25 mL three-necked flask, 0.3 g $SnBr_2/BiBr_3$ was placed in equal volume (7.5 mL) of OA and OLA and heated under nitrogen flow to 200 °C for 1 h for the $SnBr_2/BiBr_3$ to completely dissolve. Thereafter, using a syringe, 1 mL of CsOA was injected quickly into the three-necked flask containing $SnBr_2/BiBr_3$ for 1 min. Thereafter, using a cold-water bath, the flask was cooled to room temperature. Subsequently, the resultant nanoparticles were washed multiple times in toluene and hexane.

2.3. Schottky Diode Fabrication

Prior to the device fabrication, the ITO-coated glass substrate was washed using the ultrasonic bath in ethanol, acetone, and distilled water for 15 min each. The ITO glass substrates were then dried. The device structure consisted of ITO/perovskite/Au thin film layers. The device was obtained by spin-coating the well-dispersed solution of the perovskite nanocrystals in hexane on the ITO substrate at 3000 rpm for 2 min. The film was then dried at 90 °C. The process was repeated six times to get an approximate thickness of 200 nm or more.[23] The top Au contact was thermally deposited through a shadow mask to form an array of patterned electrodes. The Au was deposited in a high vacuum with pressure exceeding 4×10^{-5} Pa, current of 280 A and voltage of 80 kV on a device with an active area of 0.05 cm^2. A Keithley 2400 source meter was used to measure the I–V of the Schottky device in the dark at 298 K.

2.4. Characterization

A Bruker D2 phaser diffractometer equipped with a Cu Kα radiation source (λ 1.541060 Å) at 30 kV and 10 mA was used for the powder X-ray diffraction (PXRD) analysis. The measurements were acquired over the range of 10–60° at ambient temperature with a step size of 5 s. The absorption measurements were performed using a Specord 210 plus AnalytikJena UV-vis spectrophotometer after the nanoparticles were dispersed in toluene and then placed in a quartz cuvette (1 cm path length). A HORIBA QM8000 spectrofluorometer with a PPD-850 detector was used for photoluminescence measurements on the powdered samples. Using a FEI Technai T12 transmission electron microscope (TEM), which was operated at 120 kV with a beam spot of 3, the perovskites morphologies were determined. Prior to analysis, the nanocrystals were dispersed in toluene and drop-casted onto a lacey-carbon copper grid which was then dried at room temperature. X-ray photoelectron spectroscopy (XPS) analysis was conducted using a physical electronics PHI 5700 spectrometer equipped with non-monochromatic Mg Kα X-rays (300 W, 15 kV, and 1253.6 eV) as the excitation source. The spectrometer energy scale was calibrated using Cu $2p_{3/2}$, Ag $3d_{5/2}$, and Au $4f_{7/2}$ photoelectron lines at 932.7, 368.3, and 84.0 eV, respectively. Before being moved to the analysis chamber for characterization, the samples were loaded on a sample holder and stored overnight at high vacuum in the preparation chamber. The spectra were collected in the constant pass energy mode at 29.35 eV. The residual pressure in the analysis chamber was maintained below 1.33×10^{-7} Pa during the spectra acquisition. The thermal stability of the samples was monitored with a PerkinElmer 6000 thermogravimetric analyzer. The scanning electron microscope (SEM) micrographs of the perovskite film layers were collected using a TESCAN Vega SEM equipped with a tungsten filament. The $I-V$ measurement for the Schottky device was performed in the dark at 298 K using a Keithley 2400 source meter. The electrical impedance spectroscopy (EIS) measurements were carried out between 0.1 and

0.1 MHz using a Biologic SP 300 potentiostat. The impedance plots were fitted using Biologic Z-fit software for proper equivalent circuit models.

3. Results and Discussion

The crystal phases and presence of impurities in the synthesized nanocrystals were determined using powder X-ray diffraction (PXRD). **Figure 1** shows the PXRD patterns of the $CsSnBr_3$ and $Cs_3Bi_2Br_9$ perovskite nanocrystals synthesized at 230 and 210 °C, respectively. The $CsSnBr_3$ and $Cs_3Bi_2Br_9$ NCs crystallize in the cubic and hexagonal phases, respectively. The Sn perovskite corresponds to reference card PDF 01-070-1645 with a lattice parameter of $a = 5.79500$ Å, while the Bi perovskite corresponds to reference card PDF 01-070-0493 with lattice parameters $a = 7.97200$ Å and $c = 9.86700$ Å. For both perovskites, all the peaks in the XRD patterns match the reference peaks, indicating phase purity. A slight shift observed in both patterns suggests the presence of defects in the materials.[24]

Prior to this study, the colloidal synthesis of $CsSnBr_3$ has mostly relied on the use of the expensive trioctylphosphine (TOP) as the reducing and coordinating solvent. Other methods employ additional precursors such as $MgBr_2$.[8,9] The sole use of an oleylamine (OLA) and oleic acid (OA) mixture has been reported to form CsBr precipitate instead of the desired $CsSnBr_3$.[8] However, in this study, by using an appropriate synthesis temperature along with the suitable volumes of OLA and OA only, $CsSnBr_3$ perovskite can be synthesized without the need for TOP or any additional precursors. This results in a cost-effective method for the synthesis of lead-free perovskites.

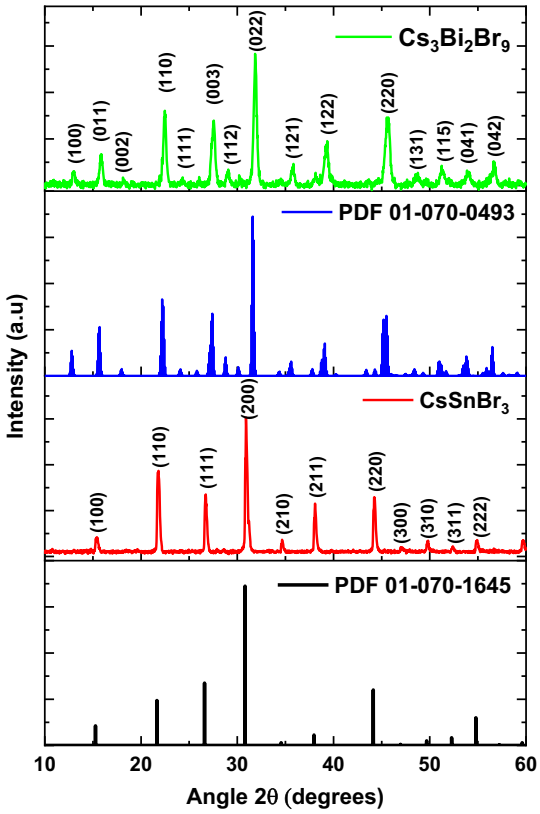

Figure 1. XRD patterns of $CsSnBr_3$ and $Cs_3Bi_2Br_9$ nanocrystals.

The UV-vis absorption and emission spectroscopies were employed to investigate the optical characteristics of the perovskite NCs, as illustrated in **Figure 2**. The bandgap energies for $CsSnBr_3$ and $Cs_3Bi_2Br_9$, determined from their excitonic peaks, are 1.82 and 2.83 eV, respectively. The presence of these excitonic peaks indicates samples with minimal defects, facilitating direct transitions of electrons from the valence band to the conduction band. However, the slight broadening of the peaks suggests the presence of some defects. For a comprehensive understanding of defect formation, photoluminescence spectroscopy serves as an excellent tool.[25] The red shifting of the emission spectrum relative to the absorption spectrum is typically attributed to radiative losses. Specifically, the emission maxima for the Sn and Bi perovskites are observed at 1.78 and 2.59 eV, respectively. The small Stokes shift indicating near band edge emission suggests minimal defects; however, the broadening of the peaks with a full width at half maximum (FWHM) of ≈100 nm indicates the presence of some defects.[26]

Figure 3 shows the TEM and HRTEM images as well as the size distribution of the Sn and Bi-based perovskites. Spherical and pseudospherical morphologies were obtained for $CsSnBr_3$ and $Cs_3Bi_2Br_9$ NCs, respectively. The particles are well-dispersed and appear to be monodispersed. The HRTEM image of $CsSnBr_3$ shown in Figure 3b displays lattice fringes with a d-spacing of 0.272 nm corresponding to the (110) crystal plane of a cubic phase perovskite. This agrees with the PXRD pattern, although it is slightly shifted, suggesting lattice strain. Additionally, some vacancies are observed in the lattice fringes, indicating the presence of defects. This observation is consistent with the optical properties. The NCs have an average particle size of 2.3 ± 1 nm, as shown in the histogram (Figure 3c). On the contrary, the Bi-based NCs exhibit sparsely distributed uniform particles. The HRTEM in Figure 3c shows lattice fringes with a d-spacing of 0.234 nm corresponding to the (110) lattice plane. Similar to the Sn-based perovskite, the d-spacing is slightly different from the PXRD d-spacing for a hexagonal phase perovskite, suggesting lattice strain and the presence of defects. The $Cs_3Bi_2Br_9$ NCs have an average particle size of 17 ± 2 nm. The smaller standard deviation indicates more monodispersed particles, which aligns with the more pronounced UV-vis excitonic peak.

XPS was carried out on the perovskites (**Figure 4** and **5**). The survey spectrum of $CsSnBr_3$ and $Cs_3Bi_2Br_9$ are shown in Figure S1 and S2 (Supporting Information), respectively. As a result of spin–orbit coupling, the Cs 3d and Sn 3d give two peaks while the chemical environment of each constituent element is probed by deconvoluting their spectra. The high-resolution spectrum of Cs 3d (Figure 4a) shows two peaks at 724.5 and 738.4 eV attributed to $3d_{5/2}$ and $3d_{3/2}$ of Cs^+.[27] Additionally, the doublet separation of these peaks is 13.9 eV, which agrees with the standard peak separation of Cs 3d.[27,28] The Sn 3d spectrum shows two distinct peaks at 486.8 eV ($3d_{5/2}$) and 495.2 eV ($3d_{3/2}$).[29] The doublet separation of the two Sn 3d peaks is 8.44 eV, which is in good agreement with the literature.[30] The Sn (Figure 4b) 3d peak at 486.8 eV is attributed to $SnBr_2$ bonding, while the peak seen at 495.2 eV is assigned to SnO_2, indicating the oxidation of Sn in the $CsSnBr_3$ NCs.[31] Gupta et al.[32] synthesized cubic

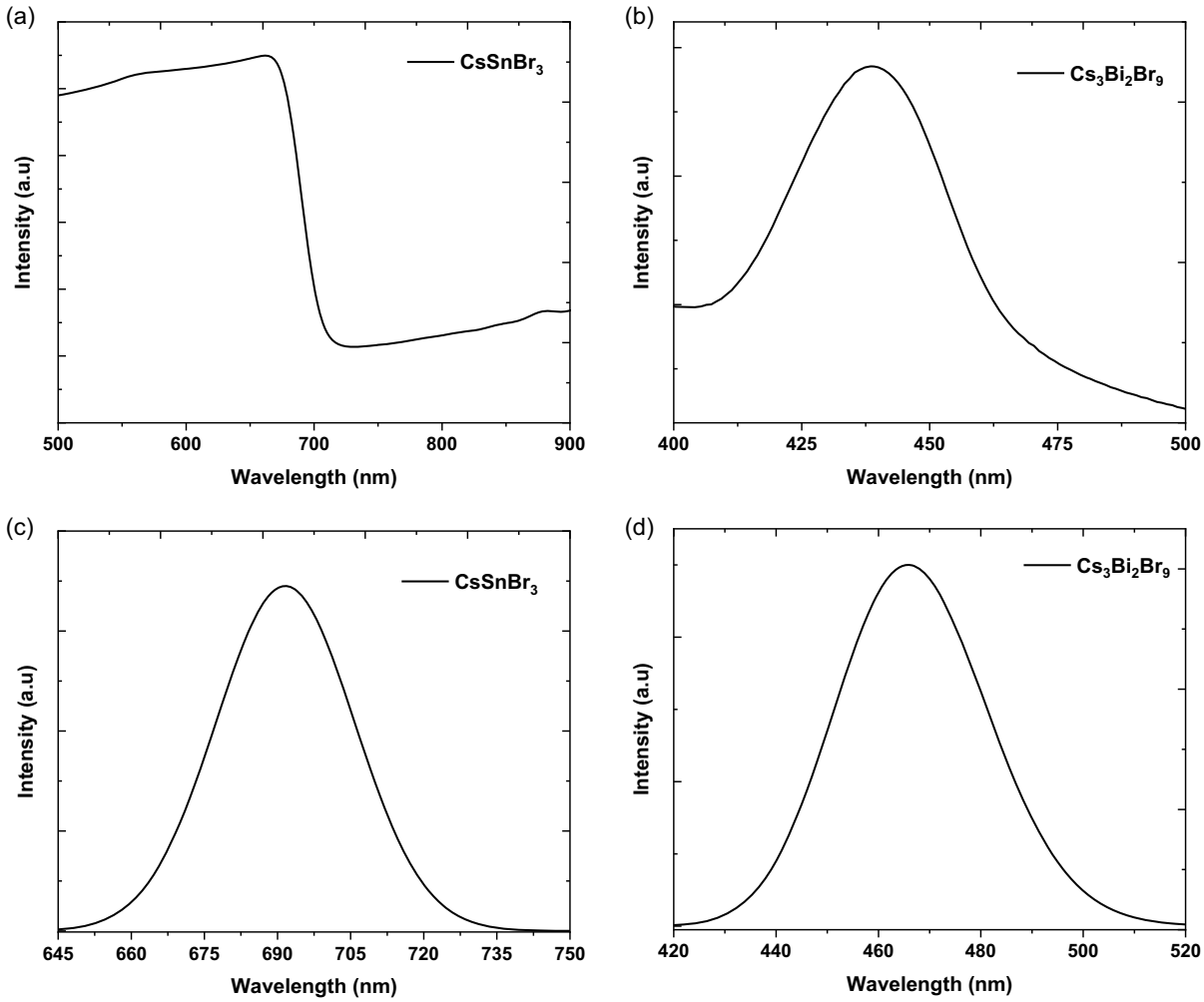

Figure 2. a,b) UV-vis spectra of $CsSnBr_3$ and $Cs_3Bi_2Br_9$, c,d) photoluminescence spectra of $CsSnBr_3$ and $Cs_3Bi_2Br_9$ nanocrystals ($\lambda_{exc} = 400$ nm and 300 nm, respectively).

$CsSnBr_3$ perovskite NCs and, upon irradiation with the X-ray beam of the XPS, the material showed susceptibility to beam damage due to the generation of additional peaks at 493 and 484.5 eV. These peaks were attributed to the formation of Sn^0; therefore, to improve their perovskite's stability, SnF_2 was added. It is noteworthy that such beam damage was not observed during our characterization, as aside from the expected double peaks of Sn 3d, no additional peaks are observed in our sample, as confirmed in Figure 4b. The high-resolution Br 3d spectrum (Figure 4c) is deconvolved into two peaks at 68.2 eV ($3d_{5/2}$) and 69.3 eV ($3d_{3/2}$), where both peaks are attributed to the CsBr bonding in the sample.[17] The high-resolution O 1s spectrum peak (Figure 4d) is deconvoluted into two peaks at 530.7 and 532.2 eV, where the peak at 530.7 eV is attributed to the metal oxide while organic C–O is responsible for the peak observed at 532.2 eV. The metal oxide is attributed to the oxidation of Sn^{2+} to Sn^{4+} as opposed to cesium, as tin is more reactive.[33] The organic assignments (Table S1, Supporting Information) are attributed to the capping ligands on the surface.

From the $Cs_3Bi_2Br_9$ XPS analysis (Figure 5), the deconvoluted Cs 3d spectrum shows two distinct peaks at 724 and 738 eV corresponding to the $3d_{5/2}$ and $3d_{3/2}$ of Cs^+. The Bi 4f spectrum shows peaks centered at 158.7 and 164.1 eV, correlating to the $4f_{7/2}$and $4f_{5/2}$ of the Bi^{3+} ions. The f-level spin–orbit split for Bi is 5.4 eV, which is in agreement with previous literature. The high-resolution Br 3d spectrum is deconvoluted to two peaks at 68.2 eV (Br $3d_{5/2}$) and 68.8 eV (Br $3d_{3/2}$) that both correspond to the CsBr bonding in the material.[28] The O 1s spectrum shows three deconvoluted peaks at 529.4, 531, and 533 eV, corresponding to the metal oxide, C—O, and C═O interactions in the sample, respectively.[28] In the case of $Cs_3Bi_2Br_9$, the metal oxide is attributed to the formation of a thin layer of Bi_2O_3.[34] The presence of metal oxides (Table S1 and S2, Supporting Information) for both $CsSnBr_3$ and $Cs_3Bi_2Br_9$ is indicative of the lack of stability of these nanocrystals.

TGA was done to determine the thermal stability of the perovskite NCs. From the TGA curves in **Figure 6**a, the derivative weight curve shows two distinct decomposition peaks of the $CsSnBr_3$ NCs where the maximum temperatures for the two

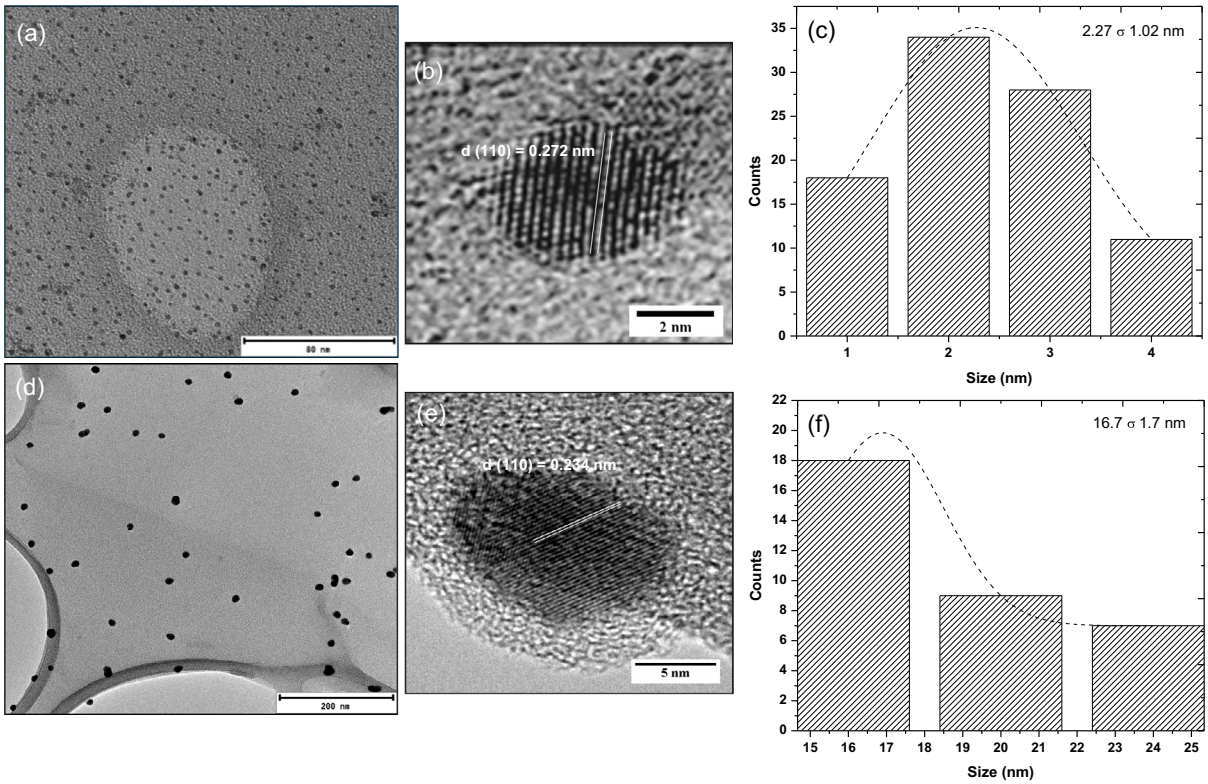

Figure 3. TEM and HRTEM images of a,b) $CsSnBr_3$, d,e) $Cs_3Bi_2Br_9$ and size distribution of c) $CsSnBr_3$, f) $Cs_3Bi_2Br_9$ perovskite nanocrystals.

decompositions are at 461 and 832 °C. The weight percent curve shows that about 38.9% of the perovskite's weight was lost during the first decomposition step while 43.7% weight was lost during the second decomposition process. The first decomposition of the $CsSnBr_3$ perovskite NCs is due to the decomposition of the surface organic molecules since the TGAs of both OLA and OA have been reported to decompose at a temperature range of 300–450 °C.[27] The second decomposition at a higher temperature may be attributed to CsBr degradation in the material. CsBr has a molar mass of 212.80 g mol^{-1}, using proportionality, the 43.67% weight loss observed in the second decomposition process accounts for 214.5 g mol^{-1} of the total 491.32 g mol^{-1} molar mass of the $CsSnBr_3$ NCs. Also, CsBr sublimes at 650 °C and this corresponds to the onset region of the second degradation curve.

For the $Cs_3Bi_2Br_9$ TGA (Figure 6b), the derivative weight curve shows four decomposition peaks of the $Cs_3Bi_2Br_9$ NCs where the maximum temperatures for the four decomposition steps are located at 330, 567, 632, and 839 °C. The weight percent curve shows that about 8.5% of the perovskite's weight was lost during the first decomposition step; this initial decomposition can be due to the loss of moisture in the sample. Furthermore, the second and third decomposition steps starting at about 455 °C occur simultaneously as revealed by the derivative weight curve. The concomitant decomposition processes may be due to $BiBr_3$ degradation and CsBr sublimation, as $BiBr_3$ has a boiling point of about 461 °C while CsBr sublimes at about 650 °C.[27] Finally, the last decomposition process peaking at 839 °C may be attributed to inorganic residue in the perovskite.

Perovskites are typically unstable in ambient conditions, which consequently affect their application; therefore, stability studies were performed on the $CsSnBr_3$ and $Cs_3Bi_2Br_9$ NCs. From the XRD pattern in Figure S3 (Supporting Information), the crystal structure and phase of the perovskite remain unchanged for the first three days. However, by day four, secondary peaks shown as asterisks begin to appear, and finally, after 21 days, these peaks become very pronounced. The secondary peaks formed are attributed to the oxidation of Sn^{2+} to Sn^{4+} in the perovskite. Similar oxidation of Sn^{2+} to Sn^{4+} has been reported for the Sn-based perovskites.[33] However, it is significant to mention that the $CsSnBr_3$ NCs synthesized here showed improved stability in comparison to other reported $CsSnBr_3$ perovskites. For instance, Wang et al.[35] synthesized $CsSnBr_3$ NCs via colloidal synthesis, but the perovskite started degrading after 3 h and then completely decomposed after 16 h. Similarly, Moghe et al.[36] prepared $CsSnBr_3$ films, and upon exposure to ambient conditions, the perovskite was only stable for about 25 h. Contrarily, in Figure S4 (Supporting Information), $Cs_3Bi_2Br_9$ NCs exhibit impressive stability for 21 days with no observable phase deviation of the material, as evidenced by the absence of secondary peaks and lack of deviation in peak positions. This indicates that the Bi-based perovskite is more stable than the Sn-based perovskite, which was only stable for 3 days.

The perovskite nanocrystals ($CsSnBr_3$ and $Cs_3Bi_2Br_9$) were utilized as the semiconductor in a Schottky barrier diode. **Figure 7** presents the schematic diagram of the diode and SEM images of the semiconductor layer. The SEM images of $CsSnBr_3$ show no

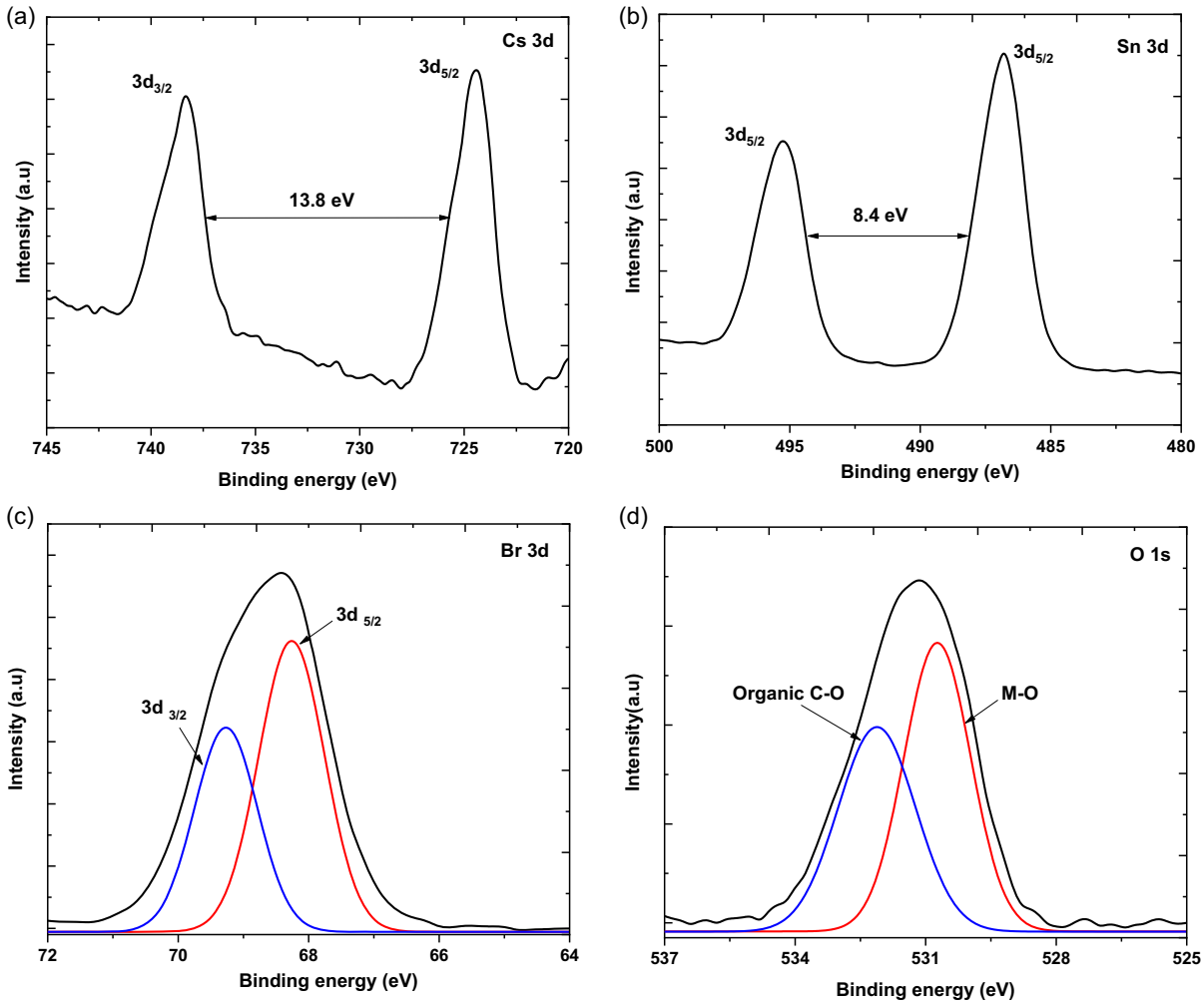

Figure 4. XPS high-resolution spectra of $CsSnBr_3$ nanocrystals showing a) Cs 3d, b) Sn 3d, c) Br 3d, and d) O 1s spectra.

pinholes; however, the particles are more polydispersed, consistent with the large standard deviation in the particle size distribution. Conversely, $Cs_3Bi_2Br_9$ displays more uniform sizes and coverage, in line with the smaller standard deviation observed in the size distribution curve as well as the pronounced excitonic absorption peak. Schottky diodes serve as valuable tools in understanding critical electrical properties relevant to solar cells. These diodes offer insights into the barrier heights at semiconductor–metal interfaces, aiding in the comprehension of charge carrier dynamics within the solar cell structure. The measured barrier height directly impacts electron and hole transport, influencing the cell's efficiency. Additionally, Schottky diodes provide data on series resistance and ideality factors, which are crucial parameters affecting the overall performance of solar cells.[27]

The Schottky barrier height ($\varnothing_B$) was determined from the *I–V* curve. From Schottky thermionic theory the relationship between the applied voltage V and the forward current I is expressed with the equation:

$$I = I_0\left[\exp\left(\frac{qV}{nk}\right) - 1\right] \quad (1)$$

where q is the electronic charge, k the Boltzmann constant, T the ambient temperature, and n is a dimensionless which indicates the deviation from the ideal Schottky cell characteristics. I_0 is the saturation current represented by Equation (2):

$$I_0 = SA^*T^2\exp\left(-\frac{q\varnothing_B}{kT}\right) \quad (2)$$

$$LnI = LnI_0 + \frac{q}{nkT}V \quad (3)$$

with $A^* = A\left(m^*/m_0\right)$, where A is the Richardson constant while the effective electron mass is represented as m^* and this is estimated to be 0.73 and 0.34 m_0 for $CsSnBr_3$ and $Cs_3Bi_2Br_9$ nanocrystals, respectively.[37,38] The saturation currents were 9.97 and 9.92 mA for the Sn and Bi-based Schottky diodes. The ($\varnothing_B$) is obtained from Equation (4) where S is the area of the cell.

$$\varnothing_B = \left(-\frac{kT}{q}\right)Ln\left(-\frac{SA^*T^2}{I_0}\right) \quad (4)$$

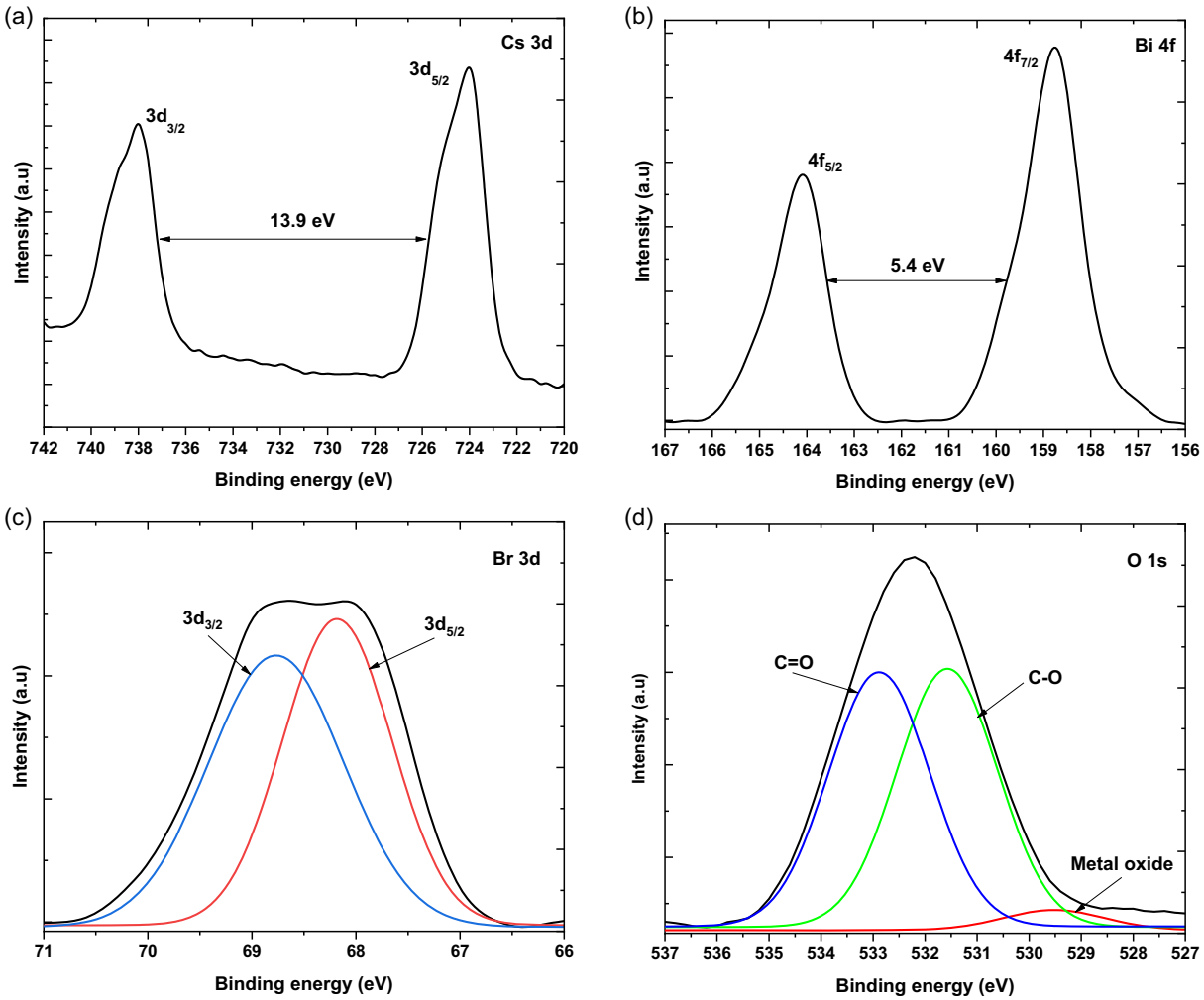

Figure 5. XPS high-resolution spectra of $Cs_3Bi_2Br_9$ nanocrystals showing a) Cs 3d, b) Bi 4f, c) Br 3d, and d) O 1s spectra.

The slope of *Ln I* versus *V* (Equation (3)) is used to evaluate the coefficient *n*. The classical thermionic method has a limitation because it only works for diodes possessing negligible series resistance (R_s) in the forward bias. However, since the series resistance (R_s) is a crucial parameter influencing the electrical behavior of a Schottky diode, other methods (Cheung and Norde) are employed to determine R_s, $Ø_B$, and n. With the Cheung's method, *n*, $Ø_B$, and R_s can be obtained. The forward bias *I–V* characteristics as a result of thermionic emission of a Schottky diode with (R_s) can be expressed as Cheung's functions:[39]

$$\frac{dV}{dLnI} = n\frac{kT}{q} + IR_s \tag{5}$$

$$H(I) = V - n\frac{kT}{q}Ln\left(\frac{1}{SA^{*2}}\right) \tag{6}$$

$$H(I) = nØ_B + IR_s \tag{7}$$

Using the straight-line plot of $dV/dLnI$ vs I, *n*, and R_s can be determined from the slope and the y-intercept with Equation (5). Moreso, another method was developed by Norde to obtain the values of the (R_s) and $Ø_B$.[40] The Norde method can be expressed as follows:

$$F(V) = \frac{V}{\gamma} - \frac{kT}{q}Ln\left(\frac{I}{SA^*T^2}\right) \tag{8}$$

where γ is a first integer greater than *n*, *I* the current obtained from *I–V*. The γ is taken to be 2 and 3 for $CsSnBr_3$ and $Cs_3Bi_2Br_9$, respectively in this study. Hence, the $Ø_B$ and (R_s) can be obtained from Equation (9) and (10).

$$Ø_B = F(V_0) + \frac{V_0}{\gamma} - \frac{kT}{q} \tag{9}$$

$$R_s = \frac{kT(\gamma - n)}{qI} \tag{10}$$

The *I–V* characteristic curves of $CsSnBr_3$ and $Cs_3Bi_2Br_9$ nanocrystals are shown in **Figure 8** and **9**, respectively. These representative *I–V* curves all show a degree of rectification which is characteristic of a Schottky barrier diode.

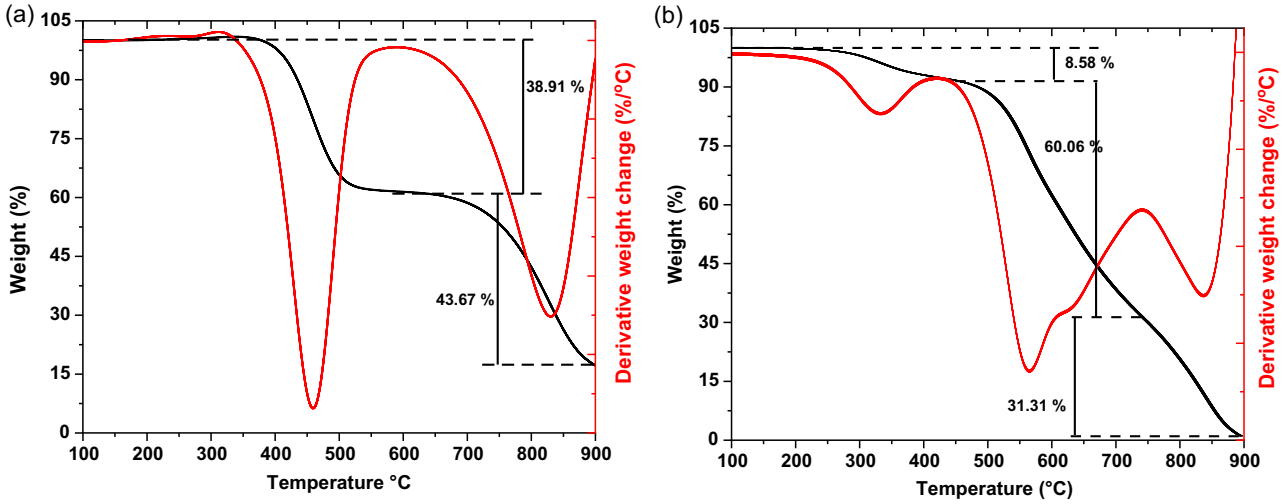

Figure 6. TGA of a) $CsSnBr_3$ and b) $Cs_3Bi_2Br_9$ perovskite nanocrystals determined after a day of synthesis.

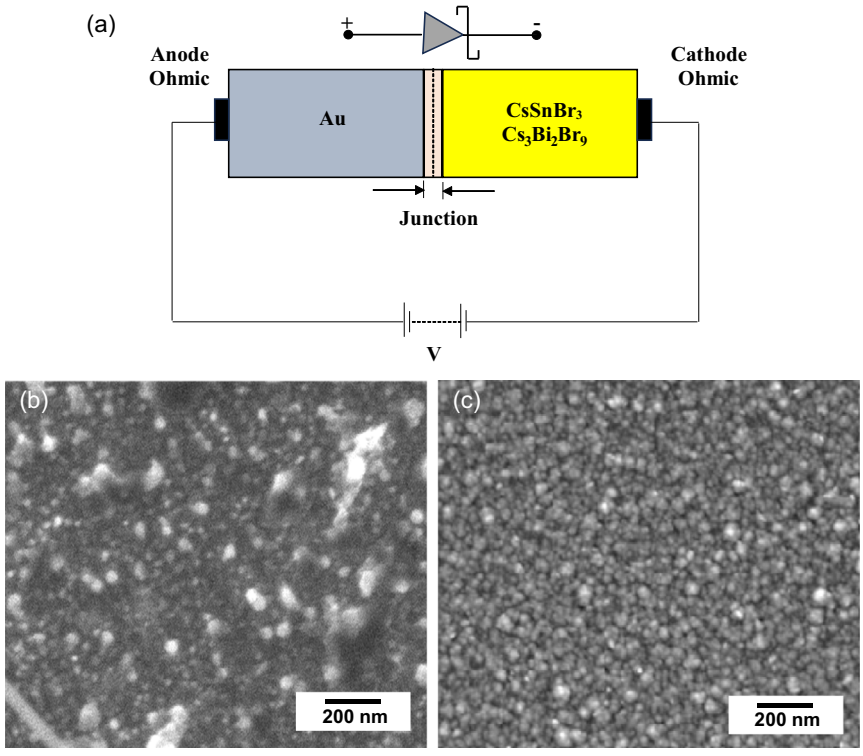

Figure 7. a) Schottky diode schematic, b) the SEM images of the $CsSnBr_3$, c) and $Cs_3Bi_2Br_9$ thin films.

The Schottky diode characteristics for the classical thermionic, Cheung and Norde's models are summarized in **Table 1**. The classical thermionic ideality factors n of the two Schottky diodes are 3.37 and 3.67 for $CsSnBr_3$ and $Cs_3Bi_2Br_9$ samples, respectively. The ideality factor of a Schottky diode indicates how well it matches the ideal diode equation, where n is a unity in an ideal diode. The n obtained for the perovskite NCs show a deviation from the ideal thermionic emission model. This deviation could be due to external factors like the presence of interface states or inhomogeneity in barrier height.[41] This deviation of n is an indication that other mechanism such as field-enhanced and thermally assisted tunneling contribute to the current transport in the system.[42] Comparatively, an ideality factor of 4.84 was obtained in the hybrid organic–inorganic Pb-based perovskite Schottky diode,[43] which is higher than the n obtained for the Sn and Bi perovskite. The n, were also determined with the Cheung's method using Equation (6) and (7). From Cheung's function, n, are 1.3 and 2.5 for $CsSnBr_3$ and $Cs_3Bi_2Br_9$,

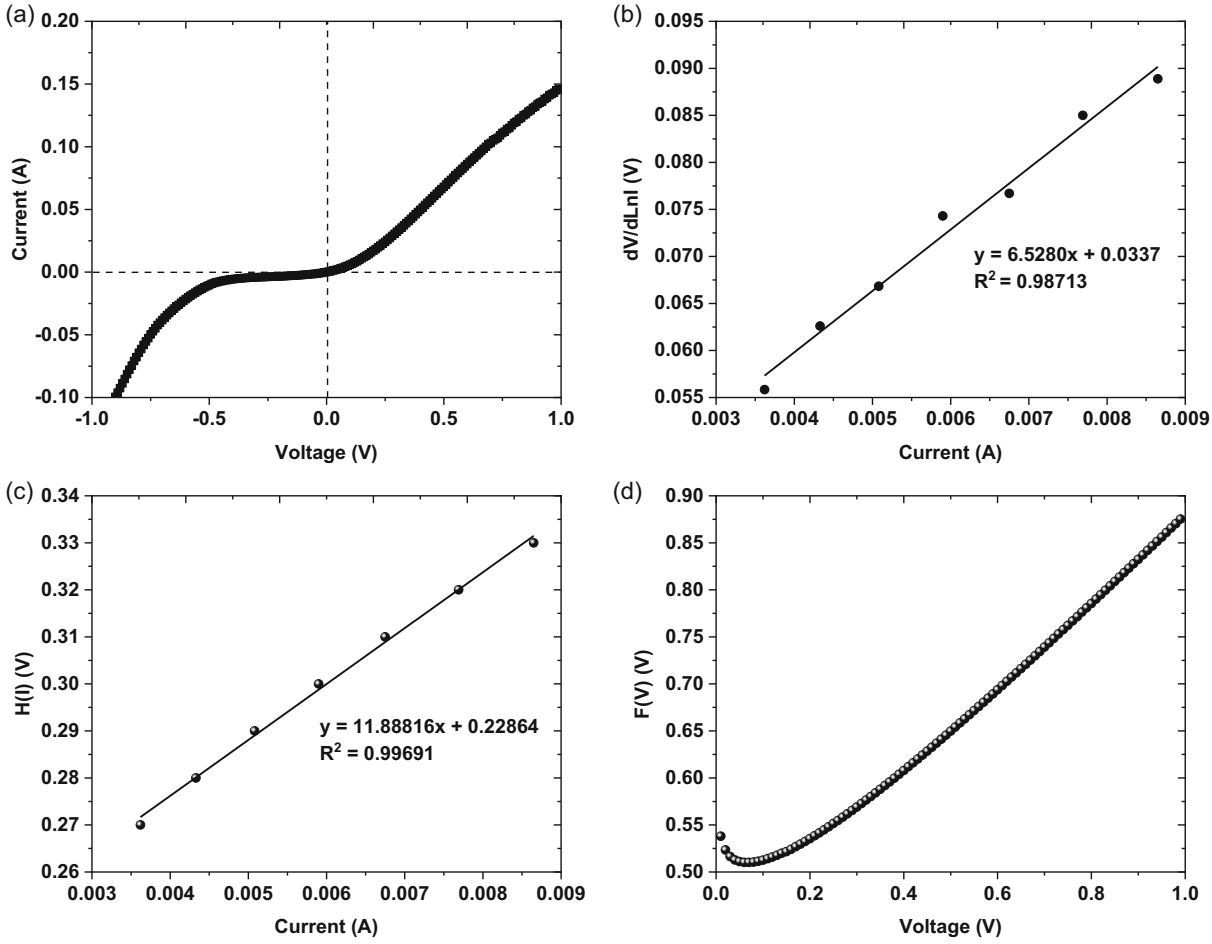

Figure 8. a) *I–V*, b) *dV/dLnI–I*, c) *H(I)−I*, and d) *F(V)–V* characteristics of the Au/$CsSnBr_3$ Schottky diode at the temperature of 298 K in the dark.

respectively. This indicates that moderately good junctions are formed for the $CsSnBr_3$ and $Cs_3Bi_2Br_9$. Shaikh et al.[44] employed $CH_3NH_3PbBr_3$ perovskite for a Schottky diode, using the Cheung's method, an ideality factor of 1.7 was observed, this n is comparable to the one obtained for the Sn-based perovskite. This suggests that the synthesized $CsSnBr_3$ perovskite NCs may be used as replacement for Pb-based perovskite materials. Due to presence of defects and generation-recombination currents within the space charge region, high bandgap heterojunctions often possess high ideality factor.[27] As a result, from both the classical thermionic and Cheung's method a concomitant increase in n was observed as the bandgap energy increases from $CsSnBr_3$ to $Cs_3Bi_2Br_9$.

The extent of the energy mismatch is expressed by $Ø_B$, which reflects the energy position between the semiconductor's band edge and the metal's Fermi level.[45] The $Ø_B$ was found to steadily decrease from 0.330 to 0.313 eV for the $CsSnBr_3$ and $Cs_3Bi_2Br_9$ based Schottky diodes, respectively using the thermionic model. Similar decrement was observed in both the Cheung and Norde's model where $Ø_B$ of 0.174 and 0.117 eV are obtained for the Sn and Bi perovskites using the Cheung's method. While $Ø_B$ of 0.785 and 0.462 eV are obtained for $CsSnBr_3$ and $Cs_3Bi_2Br_9$ Schottky diodes using the Norde's model. This steady decrease in $Ø_B$ from $CsSnBr_3$ to $Cs_3Bi_2Br_9$ nanocrystals can be attributed to surface oxidation. The $Ø_B$ is usually influenced by surface oxidation where $Ø_B$ increases linearly with oxide thickness.[46,47] Hence, it is unsurprising that the easily oxidized perovskite ($CsSnBr_3$) possessed the highest $Ø_B$. This effect of oxide thickness on $Ø_B$ is due to the charges trapped in the oxide layer which alters the semiconductor's charge distribution by forming a dipole layer with the charges confined in the surface states.[48] This results in a potential shift that alters the $Ø_B$. Although Schottky diodes based on perovskite semiconductors have barely been reported, however, a barrier height of 0.97 eV was reported for an organo-lead halide perovskite Schottky photodiode.[49] Liu et al.[50] fabricated a high-efficiency graphene-on-silicon Schottky junction solar cell, the undoped device showed an ideality factor of 3.39 while the doped material which has the highest efficiency had an ideality factor of 1.50. Both the pristine and doped material had $Ø_B$ of 0.76 and 0.87 eV. These values are comparable to the ones obtained for the perovskites herein which further accentuate the potential of Sn and Bi as Pb substitute in perovskites.

The R_s obtained from the Cheung's method are 6.528 and 11.888 Ω for $CsSnBr_3$ NCs while R_s of 6.393 and 10.774 Ω is obtained for $Cs_3Bi_2Br_9$ NCs. However, the Norde's method gives R_s values of 6.040 and 2.047 Ω for Sn and Bi-based Schottky

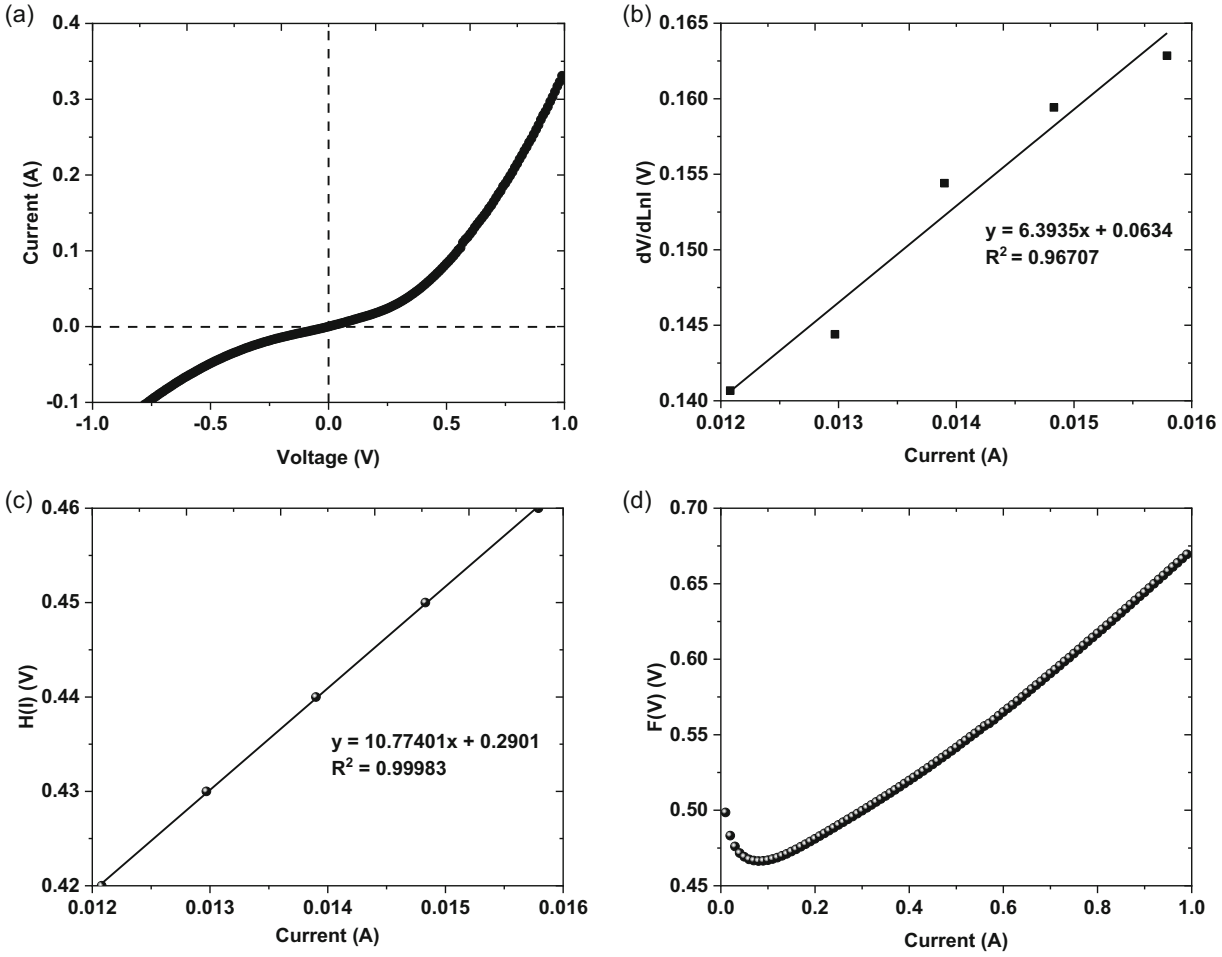

Figure 9. a) *I–V*, b) *dV/dLnI–I*, c) *H(I)−I*, and d) *F(V)–V* characteristics of the Au/$Cs_3Bi_2Br_3$ Schottky diode at the temperature of 298 K in the dark.

Table 1. Diode parameters obtained from the *I–V* data of $CsSnBr_3$ and $Cs_3Bi_2Br_9$ perovskite nanocrystals.

Material	Method	Ideality factor, *n*	Barrier height, $Ø_B$	Series resistance, R_s
$CsSnBr_3$	*LnI–V*	3.370	0.330 eV	–
	dV/dLnI–I	1.300	–	6.528 Ω
	H(I)–I	–	0.174 eV	11.888 Ω
	F(V)–V	–	0.785 eV	6.040 Ω
$Cs_3Bi_2Br_9$	*LnI–V*	3.670	0.313 eV	–
	dV/dLnI–I	2.500	–	6.393 Ω
	H(I)–I	–	0.117 eV	10.774 Ω
	F(V)–V	–	0.462 eV	2.047 Ω

diodes respectively. The R_s is among the parasitic resistances that influences a Schottky diode's *I–V* characteristics. Determining this parameter offers information on the Schottky device's performance. Although there are no set limits for R_s, however, low R_s is essential for optimal solar cell performance.[51] Furthermore, when the series resistance is high, determining the diode parameters particularly the $Ø_B$ becomes difficult.[52] The R_s obtained from both Cheung's and Norde's method steadily increases from $Cs_3Bi_2Br_9$ to $CsSnBr_3$. Of the two materials, $CsSnBr_3$ shows the highest series resistance. The trend can be due to the oxidation of the perovskite NCs either prior to film deposition or during the metal deposition. This oxidation creates an oxide layer at the metal–semiconductor interface, resulting in an interface state charge that can influence the diode's electrical properties.[53] This idea was further substantiated by the XPS data for the individual perovskites. From the XPS spectra of $CsSnBr_3$, and $Cs_3Bi_2Br_9$, the obtained atomic % of oxygen in the sample were 25.2% and 8.5%, respectively (Table S1 and S2, Supporting Information). Hence, this steady decrease in oxygen content from Sn to Bi perovskite as recorded via XPS analysis directly corresponds to the decrease in series resistance observed for the different materials. Finally, the values obtained from Norde's functions differ from those obtained from Cheung's methods, because the Cheung's functions only apply to the nonlinear region of forward bias *I–V* curve while Norde's functions are executed for the entire forward bias region of the diode's *I–V* curve.

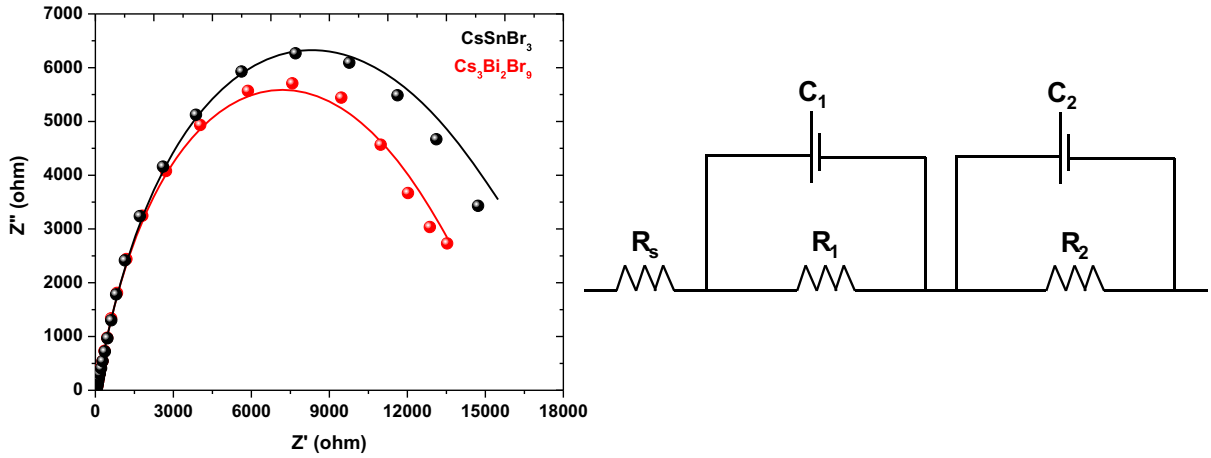

Figure 10. Nyquist plot of $CsSnBr_3$ and $Cs_3Bi_2Br_9$ and the equivalent circuit.

Table 2. Different parameters obtained from fitting of Nyquist curves by EIS spectrum analysing software.

Sample	R_s [Ω]	R_1 [Ω]	R_2 [Ω]	C_1 [F]	C_2 [F]	R_1C_1 [s]	R_2C_2 [s]
$CsSnBr_3$	41.43	14 435	15 774	2.91×10^{-10}	0.72×10^{-9}	4.2×10^{-6}	1.14×10^{-5}
$Cs_3Bi_2Br_9$	41.18	11 487	12 302	2.44×10^{-10}	1.13×10^{-9}	2.8×10^{-6}	1.39×10^{-5}

To further study the electrical properties, EIS was performed on the two diodes, and the Nyquist plots along with the best fit generated from the equivalent circuit are shown in **Figure 10**. From the Nyquist plots, $CsSnBr_3$ exhibited the largest electrical impedance compared to $Cs_3Bi_2Br_9$, as indicated by the larger semicircle, consistent with the electrical data from the I/V measurements. To further analyze the impedance spectra, the junctions are represented by an equivalent circuit consisting of multiple resistive and capacitive (RC) networks formed at different metal–semiconductor interfaces and a small series resistance. According to this equivalent circuit, the complex AC impedance (Z) can be expressed as:[54]

$$Z(\omega) = Z'(\omega) - iZ''(\omega) \tag{11}$$

where ω is the angular frequency of the applied sinusoidal voltage, Z′ and Z″ are the magnitudes of real and imaginary parts of the impedance, respectively. Z′ and Z″ can be expressed in terms of their constituent elements as:[54]

$$Z'(\omega) = \frac{R_1}{1 + (\omega R_1 C_1)^2} + \frac{R_2}{1 + (\omega R_2 C_2)^2} + R_s \tag{12}$$

$$Z''(\omega) = \frac{\omega R_1^2 C_1}{1 + (\omega R_1 C_1)^2} + \frac{\omega R_2^2 C_2}{1 + (\omega R_2 C_2)^2} \tag{13}$$

where R_1C_1 likely represents the interfacial Schottky junction formed between the ITO and perovskite and R_2C_2 represents the other junction formed between Au and perovskite interface.

The individual values of resistors and capacitors obtained as fitting parameters are presented in **Table 2**. Both $CsSnB_3$ and $Cs_3Bi_2Br_9$ showed low series resistance (R_s), signifying minimal resistive losses in the contacts.[55] The larger R_1 and R_2 values for $CsSnBr_3$ compared to $Cs_3Bi_2Br_9$ suggest that $CsSnBr_3$ has lower charge carrier mobility, higher interface resistance, more defects or traps, and lower overall conductivity. For both devices, C_1 being smaller than C_2 suggests that the region associated with C_1 has a thicker or more uniform depletion region due to local variations in material properties or thickness.[56] Additionally, the faster R_1C_1 time constant compared to R_2C_2 in both devices indicates that the region or process associated with R_1C_1 has faster charge dynamics, possibly due to better material properties, higher carrier concentration, or more efficient interfaces, making it better suited for high-speed or high-frequency applications.[57]

4. Conclusion

Lead-free all-inorganic perovskite nanocrystals were synthesized via colloidal synthesis. XPS analysis confirmed the composition of $CsSnBr_3$ and $Cs_3Bi_2Br_9$ and the capping of the nanocrystals. XRD and TGA results indicated that $CsSnBr_3$ was stable for 3 days before Sn^{2+} oxidation, with significant decomposition starting at 364 °C, while $Cs_3Bi_2Br_9$ nanocrystals remained stable for 21 days under standard conditions, with thermal degradation observed after 250 °C. Schottky diode parameters were determined using the classical thermionic emission model, Cheung's model, and Norde's model, revealing that surface oxidation greatly influences barrier heights and series resistance. The $Cs_3Bi_2Br_9$-based Schottky diode exhibited superior electrical properties, with the lowest series resistance and a favorable barrier height as extrapolated from Cheung's and Norde's models. EIS measurements showed that $CsSnBr_3$ has higher resistances and lower capacitances than $Cs_3Bi_2Br_9$, indicating lower charge carrier mobility and more defects, although the R_1C_1 regions in

both materials demonstrated faster charge dynamics, making them suitable for high-speed applications.

Supporting Information

Supporting Information is available from the Wiley Online Library or from the author.

Acknowledgements

The authors' appreciation goes to University of the Witwatersrand, School of Chemistry, the Wits Microscopy and Microanalysis Unit, and the National Research Foundation (NRF–Reference: SARCI1708082259148-PR-2023) for their support.

Conflict of Interest

The authors declare no conflict of interest.

Data Availability Statement

The data that support the findings of this study are available from the corresponding author upon reasonable request.

Keywords

$Cs_3Bi_2Br_9$, $CsSnBr_3$, perovskite, Schottky barrier diode

Received: December 12, 2023
Revised: August 20, 2024
Published online: October 28, 2024

[1] J. Gong, C. Li, M. R. Wasielewski, *Chem. Soc. Rev.* **2019**, *48*, 1862.
[2] M. Grätzel, *Acc. Chem. Res.* **2017**, *50*, 487.
[3] C.-H. Chiang, Z.-L. Tseng, C.-G. Wu, *J. Mater. Chem. A* **2014**, *2*, 15897.
[4] Y. Liu, Z. Yang, S. Liu, *Adv. Sci.* **2018**, *5*, 1700471.
[5] M. Konstantakou, T. Stergiopoulos, *J. Mater. Chem. A* **2017**, *5*, 11518.
[6] W.-J. Yin, J.-H. Yang, J. Kang, Y. Yan, S.-H. Wei, *J. Mater. Chem. A* **2015**, *3*, 8926.
[7] N.-G. Park, *Mater. Today* **2015**, *18*, 65.
[8] C. Quarti, E. Mosconi, F. De Angelis, *Phys. Chem. Chem. Phys.* **2015**, *17*, 9394.
[9] C. C. Stoumpos, L. Mao, C. D. Malliakas, M. G. Kanatzidis, *Inorg. Chem.* **2017**, *56*, 56.
[10] X.-G. Zhao, G. M. Dalpian, Z. Wang, A. Zunger, *Phys. Rev. B* **2020**, *101*, 155137.
[11] F. Giustino, H. J. Snaith, *ACS Energy Lett.* **2016**, *1*, 1233.
[12] K. A. Winship, *Adverse Drug React. Acute Poisoning Rev.* **1988**, *7*, 19.
[13] M. Leng, Z. Chen, Y. Yang, Z. Li, K. Zeng, K. Li, G. Niu, Y. He, Q. Zhou, J. Tang, *Angew. Chem., Int. Ed.* **2016**, *55*, 15012.
[14] R. Wang, H. Li, H. Sun, *Encyclopedia of Environmental Health*, Elsevier, Amsterdam **2019**, pp. 415–423.
[15] Y. Zhao, X. Xiao, Y. Huo, Y. Wang, T. Zhang, K. Jiang, J. Wang, S. Fan, Q. Li, *ACS Appl. Mater. Inter.* **2017**, *9*, 18945.
[16] H. S. Yoon, H.-E. Joe, S. Jun Kim, H. S. Lee, S. Im, B.-K. Min, S. C. Jun, *Sci. Rep.* **2015**, *5*, 10440.
[17] J. Miao, S. Zhang, L. Cai, C. Wang, *Adv. Electr. Mater.* **2016**, *2*, 1500346.
[18] T. Zhang, D. Su, R.-Z. Li, S.-J. Wang, F. Shan, J.-J. Xu, X.-Y. Zhang, *J. Photonics Energy* **2016**, *6*, 042504.
[19] Z. Yang, X. Dou, S. Zhang, L. Guo, B. Zu, Z. Wu, H. Zeng, *Adv. Funct. Mater.* **2015**, *25*, 4039.
[20] T.-Y. Wei, P.-H. Yeh, S.-Y. Lu, Z. L. Wang, *J. Am. Chem. Soc.* **2009**, *131*, 17690.
[21] P.-H. Yeh, Z. Li, Z. L. Wang, *Adv. Mater.* **2009**, *21*, 4975.
[22] A. Singh, A. Uddin, T. Sudarshan, G. Koley, *Small* **2014**, *10*, 1555.
[23] F. Liu, C. Ding, Y. Zhang, T. S. Ripolles, T. Kamisaka, T. Toyoda, S. Hayase, T. Minemoto, K. Yoshino, S. Dai, M. Yanagida, H. Noguchi, Q. Shen, *J. Am. Chem. Soc.* **2017**, *139*, 16708.
[24] S. Dutta, S. Chattopadhyay, A. Sarkar, M. Chakrabarti, D. Sanyal, D. Jana, *Progr. Mater. Sci.* **2009**, *54*, 89.
[25] G. J. Wetzelaer, M. Scheepers, A. M. Sempere, C. Momblona, J. Avila, H. J. Bolink, *Adv. Mater.* **2015**, *27*, 1837.
[26] V. A. Fonoberov, K. A. Alim, A. A. Balandin, F. Xiu, J. Liu, *Phys. Rev. B* **2006**, *73*, 165317.
[27] O. Akinbami, G. N. Ngubeni, F. Otieno, R. Kadzutu-Sithole, E. C. Linganiso, Z. N. Tetana, S. S. Gqoba, K. P. Mubiayi, N. Moloto, *J. Mater. Chem. C* **2021**, *9*, 6022.
[28] O. Akinbami, R. Moepya, G. N. Ngubeni, P. Tetyana, K. P. Mubiayi, N. Moloto, *J. Photochem. Photobiol. A* **2021**, *419*, 113460.
[29] P. Grutsch, M. Zeller, T. Fehlner, *Inorg. Chem.* **1973**, *12*, 1431.
[30] M. Di Giulio, G. Micocci, A. Serra, A. Tepore, R. Rella, P. Siciliano, *Sens. Actuators B* **1995**, *25*, 465.
[31] M. Zhang, Z.-Q. Tian, D.-L. Zhu, H. He, S.-W. Guo, Z.-L. Chen, D.-W. Pang, *New J. Chem.* **2018**, *42*, 9496.
[32] S. Gupta, T. Bendikov, G. Hodes, D. Cahen, *ACS Energy Lett.* **2016**, *1*, 1028.
[33] T. Wang, F. Yan, *Chem. – An Asian J.* **2020**, *15*, 1524.
[34] Y. Baer, H. Myers, *Solid State Commun.* **1997**, *21*, 833.
[35] A. Wang, Y. Guo, F. Muhammad, Z. Deng, *Chem. Mater.* **2017**, *29*, 6493.
[36] D. Moghe, L. Wang, C. J. Traverse, A. Redoute, M. Sponseller, P. R. Brown, V. Bulović, R. R. Lunt, *Nano Energy* **2016**, *28*, 469.
[37] C. Yu, Z. Chen, J. J. Wang, W. Pfenninger, N. Vockic, J. T. Kenney, K. Shum, *J. Appl. Phys.* **2011**, *110*, 063526.
[38] K. M. McCall, Z. Liu, G. Trimarchi, C. C. Stoumpos, W. Lin, Y. He, I. Hadar, M. G. Kanatzidis, B. W. Wessels, *ACS Photonics* **2018**, *5*, 3748.
[39] S. Cheung, N. Cheung, *Appl. Phys. Lett.* **1986**, *49*, 85.
[40] H. Norde, *J. Appl. Phys.* **1979**, *50*, 5052.
[41] S. Khan, S. Halder, A. Dey, B. Dutta, P. P. Ray, S. Chattopadhyay, *New J. Chem.* **2020**, *44*, 11622.
[42] R. Nouchi, *J. Appl. Phys.* **2014**, *116*, 184505.
[43] A. Upadhyaya, C. M. S. Negi, A. Yadav, S. K. Gupta, A. S. Verma, *Semicond. Sci. Technol.* **2018**, *33*, 065012.
[44] P. A. Shaikh, D. Shi, J. R. D. Retamal, A. D. Sheikh, M. A. Haque, C.-F. Kang, J.-H. He, O. M. Bakr, T. Wu, *J. Mater. Chem. C* **2016**, *4*, 8304.
[45] A. E.-D. S. Hafez, M. Abd El-Latif, *ISRN Electron.* **2013**, *2013*, e528094.
[46] F. Hasegawa, M. Onomura, C. Mogi, Y. Nannichi, *Solid-State Electron.* **1988**, *31*, 223.
[47] C. Wei, S. Yee, *J. Appl. Phys.* **1974**, *45*, 971.
[48] M. Peckerar, *J. Appl. Phys.* **1974**, *45*, 4652.
[49] W. Luo, L. Yan, R. Liu, T. Zou, S. Zhang, C. Liu, Q. Dai, J. Chen, H. Zhou, *Semicond. Sci. Technol.* **2019**, *34*, 074004.
[50] X. Liu, X. W. Zhang, J. H. Meng, Z. G. Yin, L. Q. Zhang, H. L. Wang, J. L. Wu, *Appl. Phys. Lett.* **2015**, *106*, 233901.
[51] F. Fabregat-Santiago, G. Garcia-Belmonte, I. Mora-Seró, J. Bisquert, *Phys. Chem. Chem. Phys.* **2011**, *13*, 9083.
[52] E. Karagöz, S. F. Varol, S. Sayın, Z. Merdan, *Phys. Chem. Chem. Phys.* **2018**, *20*, 30502.

[53] İ. Dökme, *Physica B: Condens. Matter* **2007**, *388*, 10.
[54] G. Bhattacharya, N. V. P. Chaudhary, T. Adhikary, S. Aich, A. Venimadhav, *Superlattices Microstruct.* **2021**, *156*, 106958.
[55] C. Yim, N. McEvoy, H. Y. Kim, E. Rezvani, G. S. Duesberg, *ACS Appl. Mater. Interfaces* **2013**, *5*, 6951.
[56] C. Y. Zhu, L. F. Feng, C. D. Wang, H. X. Cong, G. Y. Zhang, Z. J. Yang, Z. Z. Chen, *Solid State Electron.* **2009**, *53*, 324.
[57] J. Panigrahi, R. Singh, N. Batra, J. Gope, M. Sharma, *Sol. Energy* **2016**, *136*, 412.